

**Stable distorted T phase of MSi_2N_4 ($M = Ru$ and Os)
monolayers: First-principles insights into structural, vibrational,
mechanical, electronic, and optical properties**

Mirali Jahangirzadeh Varjovi,^{1,2,*} Engin Durgun,²

Gianfranco Pacchioni,¹ and Sergio Tosoni^{1,†}

¹*Department of Materials Science, University of Milano-Bicocca,*

Via Roberto Cozzi 55, 20125 Milano, Italy

²*UNAM - National Nanotechnology Research Center
and Institute of Materials Science and Nanotechnology,*

Bilkent University, Ankara 06800, Turkey

Abstract

The recent synthesis of two-dimensional (2D) MoSi_2N_4 and WSi_2N_4 crystals has given rise to a new class of 2D materials with distinctive properties and significant potential for applications in advanced technologies. The transition metal (TM) elements can potentially be substituted with other TMs, adding the possibility of introducing new members to this emerging 2D family. In this regard, we propose three structural phases ($1H$ -, $1T$ -, and $1T'$) of $M\text{Si}_2\text{N}_4$ ($M = \text{Ru}$ and Os) monolayers and examine their structural, vibrational, mechanical, electronic, and optical properties using *ab initio* methods. The results of cohesive energies (E_C) indicate that the $1T'$ structures are energetically more favorable than their $1H$ and $1T$ counterparts. The calculated phonon spectra reveal that the $M\text{Si}_2\text{N}_4$ nanosheets in distorted $1T'$ phase are dynamically stable, while their $1H$ and $1T$ forms exhibit imaginary phonon modes, signifying vibrational instability of the systems. *Ab initio* molecular dynamics (AIMD) simulations also confirm that the $1T'$ - $M\text{Si}_2\text{N}_4$ structures remain thermally stable, even up to 600 K, without any notable structural deformations. The mechanical properties of $1T'$ structures are assessed through the computation of in-plane stiffness (Y_{2D}), Poisson's ratio (ν), and ultimate tensile strain (UTS). The intrinsic geometrical anisotropy of the $1T'$ nanosheets induces strong orientation-dependent elastic properties, and the calculated large values of Y_{2D} and high UTS indicate their rigidity and suitability for strain engineering of electronic and optical properties. The calculated electronic band structures reveal that, whereas unstable $1T$ - $M\text{Si}_2\text{N}_4$ structures exhibit ferromagnetic metal properties, the stable $1T'$ - RuSi_2N_4 and $1T'$ - OsSi_2N_4 monolayers possess a nonmagnetic semiconducting ground state with indirect band gaps of 1.40 and 1.47 eV, respectively, at the level of the HSE functional. The observed shifts from metallic characteristics in the $1T$ phase to semiconducting nature in the $1T'$ structures can be attributed to the Peierls distortion. Additionally, in accordance with the direct electronic bandgap of the $1T'$ - $M\text{Si}_2\text{N}_4$ crystals, strong optical absorption within the visible parts of the optical spectrum is estimated. Our study not only expands the family of 2D MA_2Z_4 crystals, but also introduces new members with distinctive $1T'$ geometries that exhibit promising mechanical, electronic, optical features for nanomechanical and optoelectronic, and green-energy applications.

* mirali.jahangirzadehvarjovi@unimib.it

† sergio.tosoni@unimib.it

I. INTRODUCTION

Following the successful exfoliation of single-layer (SL) graphene and the unveiling of its extraordinary properties [1], significant interest has turned towards the field of two-dimensional (2D) materials [2–5]. In the realm of 2D materials, transition metal dichalcogenides (TMDs) and transition metal nitrides (TMNs) have garnered considerable attention due to their stability and diverse electronic and optical properties, spanning characteristics from semiconducting and metallic to superconducting [6–9]. This renders them appealing for both fundamental research and advanced technological applications [10, 11]. The atomic structure of 2D TMDs and TMNs monolayers can exist in various symmetry forms at the ground state, such as honeycomb ($1H$ -phase, trigonal prismatic coordination), centered honeycomb ($1T$ -phase, octahedral lattice), or distorted T -phase ($1T'$ -phase, distorted octahedral) structures [12–14]. It has been reported that MoX_2 and WX_2 (X : S, Se, and Te) monolayers are stable structures with semiconducting features in the $1H$ phase, while the metallic $1T$ - MoX_2 and $1T$ - WX_2 monolayers have been demonstrated to be dynamically unstable [15]. These metallic monolayers undergo a transformation to the $1T'$ phase due to Peierls distortion, leading to the formation of charge density waves (CDW) [16]. Typical TMDs with the formula of MX_2 (M : TM, X : S, Se, and Te), display a diverse range of Peierls-like CDW patterns [17]. Recently, Ersan et al. conducted a theoretical investigation on the three potential structural configurations ($1H$ -, $1T$ -, and $1T'$) of RuS_2 and RuSe_2 using DFT, and their findings suggest that they are dynamically unstable in the $1H$ and $1T$ phases, while stability is only observed in the $1T'$ phase [18]. In another study, a systematic and comprehensive investigation based on first principles has been performed to explore the structural and electronic properties of a series of 2D TMNs in both T and H phases, and the obtained results provide valuable insights into the electronic features of 2D TMNs [14].

In the pursuit of realizing stable TMNs through both experimental and theoretical attempts, 2D layered crystals of MoSi_2N_4 have been successfully synthesized via an innovative chemical vapor deposition (CVD) technique [19]. This exotic crystal can be regarded as a MoS_2 -like MoN_2 layer saturated by Si-N layers on both surfaces, forming a septuple atomic layer 2D material. Incorporating Si atoms in the CVD process effectively neutralizes the dangling surface bonds of MoN_2 , facilitating the growth of centimeter-scale MoSi_2N_4 nanosheets. The fabricated MoSi_2N_4 crystal is an indirect-band-gap semiconductor (1.94

eV) with high tensile strength and robust stability under ambient conditions [19]. In addition, the growth of WSi_2N_4 crystals has been reported using an approach similar to that employed for the synthesis of the MoSi_2N_4 monolayer [19]. Following this experimental achievement, a new family of 2D materials with a general formula of MA_2Z_4 is proposed [20–22]. Various 2D compounds within this family, where M represents a transition metal (Cr, Mo, W, V, Nb, Ta, Ti, Zr, Hf, Pd, and Pt), A is either Si or Ge, and Z can be N, P, or As, have been predicted and characterized using *ab initio* methods [21, 23–27]. It has been found that the electronic and magnetic properties of MA_2Z_4 monolayers vary depending on their atomic components. For instance, while the MoSi_2N_4 and WSi_2N_4 monolayers are non-magnetic semiconductors [28], the ScSi_2N_4 nanosheet is a half-metal with in-plane magnetic anisotropy [29], $\text{In}_2\text{Si}_2\text{N}_4$ crystal is a non-magnetic direct bandgap semiconductor [30], and the TaSi_2N_4 crystal is characterized as a metal and a type-I Ising superconductor [31]. In addition to the atomic components, the atomic configurations of materials also play an essential role in determining the stability and electronic properties of MA_2Z_4 structures. As an example, the $1H$ - WSi_2N_4 monolayer is a stable wide-bandgap semiconductor [32], while the metallic $1T$ - WSi_2N_4 is dynamically unstable [33], and the stable $1T'$ - WSi_2N_4 nanosheet exhibits semimetallic behavior [34]. Furthermore, Ding and Wang conducted a systematic examination of the structural stability and electronic characteristics of $M\text{Si}_2\text{N}_4$ ($M = \text{Y} - \text{Cd}$ and $\text{Hf} - \text{Hg}$) nanosheets and identified 12 stable structures with T - or H -phase configurations [33].

Among TMs, ruthenium (Ru) and osmium (Os) have received limited attention as potential candidates for optoelectronic applications. Ru and Os are classified as noble and precious metals, and similar to W and Mo, they belong to the 4d and 5d block TMs, respectively. Ru and Os exhibit comparable electronegativities and atomic radii to those of Mo and W, respectively, suggesting a plausible feasibility for their substitution. It has been demonstrated that Ru shows high catalytic performance in many chemical reactions [35]. Recently, a thin crystal film of RuS_2 has been synthesized and is regarded as one of the promising TMDs with both fundamental and technological applications, particularly in photocatalytic water splitting, photoelectrochemical energy conversion, and serving as a cathodic catalyst in direct methanol fuel cells [36, 37]. In addition, Os can be employed in the hardening of metal alloys [38]. In a recent study, a multifunctional Ru and Os-based electrode has been synthesized and proposed for large-scale electrical energy storage [39]. So far, numer-

ous studies have been carried out on the MA_2Z_4 family, exploring various TM atoms as the core element. However, no studies have been conducted with Ru and Os as the core atoms in these structures. In light of this and motivated by encouraging results from both experimental and theoretical research on the MA_2Z_4 family, in the present work, we design and investigate the structural, vibrational, mechanical, electronic, and optical properties of $1H$ -, $1T$ -, and $1T'$ - MSi_2N_4 ($M = \text{Ru and Os}$) monolayers using first-principle methods and highlight their intriguing features. Initially, the ground-state configurations of the suggested systems are determined, and their dynamical and thermal stabilities are evaluated through phonon spectrum analysis and molecular dynamic calculations, respectively. Next, the Raman spectra of stable structures are obtained, and the associated atomic displacements of the optical phonon modes are illustrated. Subsequently, the mechanical features and electronic properties of stable $1T'$ - MSi_2N_4 monolayers are examined. Finally, through the calculation of the complex dielectric function, the optical response is studied.

II. COMPUTATIONAL METHODOLOGY

In the present study, the first-principles density functional theory (DFT) [40, 41] calculations were performed by employing projector-augmented wave (PAW) [42] pseudopotentials, as implemented in the Vienna *ab initio* simulation package (VASP) [43–46]. The electron exchange and correlation (XC) interactions for both spin-polarized and spin-unpolarized cases were parametrized by the Perdew-Burke-Ernzerhof (PBE) [47] functional within the generalized gradient approximation (GGA). In addition to GGA-PBE, electronic band structures were also calculated using the hybrid Heyd-Scuseria-Ernzerhof (HSE06) [48, 49] functional, and the obtained energy bandgaps were compared with GGA-PBE results. The HSE06 hybrid functional was designed by mixing 25% of nonlocal Fock exchange with 75% of PBE exchange and 100% of PBE correlation energy and screening length of $\lambda = 0.2 \text{ \AA}^{-1}$. The kinetic energy cutoff for plane-wave basis set was taken as 520 eV, and a vacuum layer of $\sim 15 \text{ \AA}$ is considered in the nonperiodic direction of all structures to prevent unrealistic interactions between the neighboring images. The total energy convergence threshold for electronic relaxation between two consecutive steps was set to 10^{-5} eV. All the ionic positions and lattice parameters were fully optimized until the maximum allowed Hellmann-Feynman force on each atom was less than 0.01 eV/\AA , and maximum pressure on the lattice was

reduced below 1 kbar. The Gaussian-type Fermi-level smearing approach was utilized with a smearing width of 0.05 eV. For structural relaxation, the Brillouin zone (BZ) sampling was carried out with a set of Γ -centered $16 \times 16 \times 1$ uniform k -point mesh for both the $1T$ - and $1H$ - MSi_2N_4 nanosheets, and $24 \times 12 \times 1$ k -point mesh for $1T'$ - MSi_2N_4 structures [50]. The Bader technique was employed to analyze charge transfers between individual atoms by decomposing charge density into atomic contributions [51]. Phonon band dispersions were calculated using the finite displacement method as implemented in the PHONOPY [52] code by considering $4 \times 4 \times 1$ supercells for $1T$, $1H$ and $5 \times 3 \times 1$ supercells for $1T'$ systems. To examine the thermal stability of the proposed structures, *ab initio* molecular dynamics (AIMD) simulations were conducted using a microcanonical ensemble method at constant temperatures (300 and 600 K) for an overall simulation time of 6 ps with 1 fs time step. The Raman activity of each vibrational mode was computed by deriving the macroscopic dielectric tensor at the Γ -point of the BZ using the finite-difference approach [53]. In addition, the Raman spectra were plotted using a Gaussian broadening function approach from the acquired frequencies and intensities of Raman calculations. The elastic constants of suggested crystals were calculated based on the density functional perturbation theory (DFPT) method with $36 \times 24 \times 1$ k -point grids and the plane wave cutoff energy of 700 eV. To acquire optical properties, the complex dielectric function ($\varepsilon(\omega)$) was computed by taking into account light polarization along the x and y directions, utilizing both PBE and HSE functionals.

III. RESULTS AND DISCUSSION

A. Structural Properties and Energetics

We begin by introducing the structural features of MSi_2N_4 ($M = \text{Ru}$ and Os) monolayers. The suggested systems are constructed based on the geometrical characteristics of synthesized 2D $MoSi_2N_4$ and WSi_2N_4 crystals. Depending on the coordination arrangement of the constituent atoms in the unit cells, three common structural phases, namely $1H$ -, $1T$ -, and $1T'$ can be taken into account for each nanosheet. Figs. 1(a) and 1(b) illustrate the top and side views of investigated structures together with the relevant geometrical parameters labeled on them. The primitive cell of the $1H$ - and $1T$ - MSi_2N_4 crystals is hexagonal, com-

prising seven atoms, and their symmetries belong to the D_{3h} ($P\bar{6}m2$) and D_{3d} ($P\bar{3}m1$) space groups, respectively. On the other hand, $1T'$ structures are designed using a 1×2 supercell, containing fourteen atoms within their unit cell, and possess C_{2h}^2 structural symmetry. The optimized geometrical parameters of the proposed monolayers including in-plane lattice constants (\mathbf{a} and \mathbf{b}), bond lengths between M and N atoms (d_{M-N}), and thickness (h) are summarized Table I. In both $1H$ and $1T$ phases the values of \mathbf{a} and \mathbf{b} are found to be equal, whereas in the $1T'$ form, where the unit cell has an orthorhombic unit cell (i.e., rectangular in 2D projection), the values of \mathbf{a} and \mathbf{b} differ. The lattice constants for $1H$ - RuSi_2N_4 ($1H$ - OsSi_2N_4) monolayers are calculated as 2.95 Å (2.97 Å), while for the $1T$ - RuSi_2N_4 ($1T$ - OsSi_2N_4) structures, they are found to be 2.94 Å (2.92 Å). The computed lattice constants are $\mathbf{a} = 3.00$ Å (3.03 Å) and $\mathbf{b} = 5.00$ Å (4.99 Å) for $1T'$ - RuSi_2N_4 ($1T'$ - OsSi_2N_4) monolayers, respectively. The bond lengths between M and inner N atoms (d_{M-N}) in $1H$ and $1T$ structures are identical. However, in $1T'$ monolayers, the system's distortion results in four distinct bond distances between M atoms and the inner N layer. The p_1/p_2 represents the ratio of the interatomic distances between two M atoms in the systems and can be used as an index of structural distortion. Due to the inherent structural isotropy in the $1H$ and $1T$ phases, the ratio p_1/p_2 is equal to 1. However, for distorted $1T'$ nanosheets, it becomes less than 1. A smaller value of p_1/p_2 indicates a more conspicuous structural deformation within the system. For $1T'$ - RuSi_2N_4 and $1T'$ - OsSi_2N_4 monolayers this ratio is found to be 0.81 and 0.82, respectively, which is smaller than reported values for $1T'$ - MoSi_2N_4 (0.84) and $1T'$ - WSi_2N_4 (0.83) monolayers [34]. The distorted MSi_2N_4 monolayers represent the occurrence of the Peierls transition from the $1T$ phase to the $1T'$ phase [54].

The charge partition analysis of the atoms shows that in all structures, M and Si atoms transfer charge to N atoms, as their electronegativities are lower than those of N atoms. In $1H$ and $1T$, the charge donation is symmetric, whereas in $1T'$, it is asymmetric. The average charge transfer from M to N, $\Delta\rho_{(M-N)}$ is listed in Table I and the net charge transfer among the constituent atoms in the examined monolayers is displayed in Fig. S1 of the Supplemental Material [55]. According to Bader charge analyses, the values of $\Delta\rho_{(\text{Ru}-\text{N})}$ for the $1H$ -, $1T$ -, and $1T'$ structures are 1.19, 1.29, and 1.23 e^- , respectively. In $1H$ -, $1T$ -, and $1T'$ - OsSi_2N_4 monolayers, $\Delta\rho_{(\text{Os}-\text{N})}$ is estimated to be 1.30, 1.41, and 1.37, respectively. As can be seen, $\Delta\rho_{(M-N)}$ is lower in $1T'$ structures compared to their $1T$ counterparts. Upon periodic lattice distortion, the charge density within the $1T'$ structures is modulated,

resulting in the formation of a potential CDW. It is worth noting that CDW is typically observed during the transition from an undistorted phase at a critical T_{CDW} temperature. In the present case, however, the lack of experimental structural data on these compounds and the difference in lattice morphology between the $1T$ and $1T'$ phases make it very difficult to infer the nature of the transition mechanism and the related critical temperature. Further analysis is required to fully understand these aspects. The dimensionality of a system has a significant impact on CDW, similar to its influence on various other phase transition phenomena [56]. It has been reported that materials featuring CDW states display remarkable properties in both experimental and theoretical studies, making them highly desirable for a variety of applications such as heterogeneous catalysis, ferromagnetism, and superelasticity [16, 57, 58]. The planar average of the electrostatic potential of the designed monolayers is calculated, and their variations along the x , y , and z directions are presented in Fig. S2, and Fig. S3, Supplemental Material [55]. Variation of electrostatic potential along the x and y -axis for $1H$ -, $1T$ - MSi_2N_4 monolayers are identical, correlated with their geometrical isotopy. For the $1T'$ - MSi_2N_4 structures, the lattice undergoes periodic distortion along the y direction, leading to a Peierls distortion, associated with the new superlattice. From the electrostatic potential graphs plotted along the z -axis, the work function (Φ) of the studied nanosheets can be determined using the formula $\Phi = E_{Vac.} - E_{Fermi}$, where $E_{Vac.}$ and E_{Fermi} represent the energy levels of the vacuum and Fermi level, respectively. The work function of a material represents the energy barrier between the material and free space, which hinders an electron at the Fermi level from escaping. Understanding a material's work function is imperative because it determines the behavior of electrons within the material and contributes significantly to our understanding in the field of surface science, particularly regarding corrosion rates and interfacial engineering of materials. The work functions for monolayers of $1H$ -, $1T$ -, and $1T'$ - $RuSi_2N_4$ are 3.72 eV, 4.91 eV, and 4.46 eV, respectively. On the other hand, $1H$ -, $1T$ -, and $1T'$ - $OsSi_2N_4$ crystals have Φ of 3.23 eV, 4.72 eV, and 3.79 eV, respectively. The acquired results are smaller than the reported theoretical values for $MoSi_2N_4$ (5.12 eV) [59] and WSi_2N_4 (4.94) [60] monolayers. This suggests that these systems are suitable for various applications that require a lower work function, such as electron emission applications demanding high emitted current densities from the electron source. Cohesive energy, which is defined as the amount of energy required to separate a condensed material into its constituent atoms, is a fundamental physical parameter for

analyzing the energetic stability of materials. The cohesive energy per atom (E_C) of each structure can be determined using the following equation;

$$E_C = \frac{[E_T(M) + 2E_T(\text{Si}) + 4E_T(\text{N})] - [E_T(\text{MSi}_2\text{N}_4)]}{[N_M + N_{\text{Si}} + N_{\text{N}}]} \quad (1)$$

where $E_T(M)$, $E_T(\text{Si})$, and $E_T(\text{N})$ represent the energies of individual M , Si, and N atoms, respectively; and $E_T(\text{MSi}_2\text{N}_4)$ corresponds to the overall energy of the MSi_2N_4 nanosheets. Additionally, N_M , N_{Si} , and N_{N} denote the total number of M , Si, and N elements in the unit cell, respectively. All computed E_C 's, as presented in Table I, are positive and relatively large, indicating a strong cohesion between the constituent atoms. The E_C for $1T'$ - RuSi_2N_4 and $1T'$ - OsSi_2N_4 monolayers are found to be 5.92 and 5.93 eV/atom, respectively. These values exceed those of $1T$ - RuSi_2N_4 (5.87 eV/atom) and $1T$ - OsSi_2N_4 (5.87 eV/atom) nanosheets, primarily attributed to the energy lowering as a consequence of the Peierls distortion. The higher values of E_C in $1T'$ structures compared to H and T crystals indicate that $1T'$ - MSi_2N_4 phases are energetically more favorable. Additionally, the E_C 's of the $1T'$ structures are comparable to that of the $1T'$ - MoSi_2N_4 (5.98) monolayer, indicating strong bonding between the atoms within these structures [34]. According to the results summarized in Table I, monolayers of $1H$ - RuSi_2N_4 and $1H$ - OsSi_2N_4 are found to have a nonmagnetic (NM) ground state, $1T$ - RuSi_2N_4 , and $1T$ - OsSi_2N_4 nanosheets exhibit a ferromagnetic metallic character, with net magnetic moments of 1.63 and 0.55 μ_B/cell , respectively, and T' structures show nonmagnetic properties. So far, the majority of the reported T' -CDW phases are nonmagnetic (NM). The most widely recognized examples are MoX_2 and WX_2 monolayers (X is a chalcogenide atom) [61].

B. Dynamical Stability and Vibrational Properties

After acquiring the structural properties of the investigated monolayers, their dynamical stability is examined by calculating phonon dispersions using *ab initio* lattice dynamics. In the analysis of phonon spectra, if the calculated dispersions of vibrational modes have a positive square of frequency ($\omega^2 > 0$) for all k in the first BZ, the material is considered to be dynamically stable. The presence of an imaginary frequency ($\omega^2 < 0$) in a vibrational mode indicates the absence of a restoring force against the displacement of atoms along that specific phonon mode, implying structural instability. The calculated phonon band

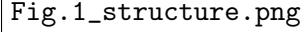
The image area is mostly blank, with the text 'Fig. 1_structure.png' located in the lower-left corner. This likely represents a missing or placeholder image for the crystal structures of MSi₂N₄ monolayers.

FIG. 1. For the three structural phases of MSi_2N_4 ($M = \text{Ru}$ and Os) monolayers (a) top and (b) side views of the crystal structures.

structures of the $1H$ -, $1T$ -, and $1T'$ - MSi_2N_4 monolayers are depicted in Fig. 2. As can be seen, the phonon spectra of $1H$ and $1T$ phases have large imaginary frequencies in nearly all directions within the hexagonal BZ, signifying dynamical instability, which is consistent with previous studies on $1H$ and $1T$ - MSi_2N_4 ($M = \text{Ru}$ and Os) structures [33]. The ground states of $1T$ nanosheets exhibit ferromagnetic metal characteristics, and we have analyzed the phonon spectra corresponding to these ground states. The imaginary frequencies are distinguished by solid red lines. For single layers of $1T'$ - RuSi_2N_4 and $1T'$ - OsSi_2N_4 , the phonon branches are free from any imaginary frequencies, indicating stability at low temperatures. The soft acoustic phonon modes in $1T$ structures are eliminated when transitioning to $1T'$ phases, a consequence of Peierls distortion within the systems. Based on a 1×2 reconstruction, the phonon spectra of $1T'$ - MSi_2N_4 crystals consist of 42 distinct vibrational modes, of which three corresponding to acoustic branches with zero frequency at Γ point, and the remaining 39 are optical branches. Due to the anisotropy of $1T'$ systems, all optical modes are nondegenerate. Among the acoustical modes, the transverse acoustic (TA) and the longitudinal acoustic (LA) branches show linear dispersions while k goes to zero. On the other hand, out-of-plane flexural acoustic (ZA) mode is parabolic near the zone center, which is a typical characteristic of the phonon spectrum of 2D materials. Additionally, the

TABLE I. For the monolayer crystals of $1H$ -, $1T$ -, and $1T'$ - MSi_2N_4 ($M = Ru$ and Os), the optimized lattice constants, \mathbf{a} and \mathbf{b} ; atomic bond length between M and N atoms, d_{M-N} ; thickness, h ; the ratio of the interatomic distance between two M atoms, p_1/p_2 ; average charge transfer from M to N , $\Delta\rho_{(M-N)}$; energy of Fermi level, E_{Fermi} ; energy level of the vacuum, $E_{\text{Vac.}}$; the calculated work function, Φ ; cohesive energy per atom, E_C ; and magnetic moment, μ .

Crystal structure	\mathbf{a} (Å)	\mathbf{b} (Å)	d_{M-N} (Å)	h (Å)	p_1/p_2 (Å)	$\Delta\rho_{(M-N)}$ (e^-)	E_{Fermi} (eV)	$E_{\text{Vac.}}$ (eV)	Φ (eV)	E_C (eV/atom)	μ (μ_B)
$1H$ - $RuSi_2N_4$	2.95	2.95	2.07	6.83	1.00	1.19	1.76	5.48	3.72	5.77	0
$1H$ - $OsSi_2N_4$	2.97	2.97	2.08	6.84	1.00	1.30	1.97	5.20	3.23	5.73	0
$1T$ - $RuSi_2N_4$	2.94	2.94	2.06	6.82	1.00	1.29	0.52	5.43	4.91	5.87	1.63
$1T$ - $OsSi_2N_4$	2.92	2.92	2.09	6.98	1.00	1.41	0.61	5.33	4.72	5.87	0.55
$1T'$ - $RuSi_2N_4$	3.00	5.00	1.96/2.05 2.06/2.14	6.82	0.81	1.23	0.94	5.40	4.46	5.92	0
$1T'$ - $OsSi_2N_4$	3.03	4.99	1.99/2.07 2.09/2.13	6.85	0.82	1.37	1.35	5.14	3.79	5.93	0

curvature of ZA modes corresponds to the ultrasonic wave propagating with the minimum group velocity. The overall characteristics of phonon band diagrams in $1T'$ - $RuSi_2N_4$ and $1T'$ - $OsSi_2N_4$ closely resemble each other. In both structures, there are frequency intervals where the optical mode coexists with acoustic phonon modes. This overlap can lead to strong acoustic and optical scattering, resulting in low thermal conductivity [62]. In $1T'$ monolayers, there are two phononic gaps formed between medium-frequency bands estimated around (480 - 510 cm^{-1}) and (685 - 700 cm^{-1}), and one in the high-frequency band (\approx 945 - 955 cm^{-1}). The presence of a phononic band gap in a material can effectively inhibit the propagation of mechanical waves at prohibited frequencies, making the material suitable for vibrational protection applications [63]. To analyze the dynamical stability of the suggested crystals under applied strain, we calculated their phonon spectrum at 6% and 10% biaxial strains. The obtained results are illustrated in Fig. S4 of the supplemental material [55]. It is observed that the monolayers maintain their dynamical stability even at high induced tensile strains of 6% and 10%. This demonstrates that the proposed materials are strain-tunable and




Fig. 2_Phonon.png

FIG. 2. Phonon spectra of $1H$ -, $1T$ -, and $1T'$ - MSi_2N_4 crystals along high symmetry directions in the 2D Brillouin zone. The phonon density of states (PhDOS) is also presented for the stable structures. Imaginary frequencies are signified by red color.

suitable for various strain-engineering applications. Additionally, applying tensile biaxial strains shifts the spectrum towards lower frequencies, corresponding to the softening of the phonon modes. We also present the phonon density of states (PhDOS) of the $1T'$ monolayers in Fig. 2. According to the PhDOS results, the major participation in the acoustic mode frequencies and low-frequency optical modes originates from the vibration of M ions due to their heavier atomic masses; however, Si and N atoms also play significant roles. The main contribution to the vibrational modes by M atoms lies within the low-energy range just below the first phonon gap. On the other hand, medium- and high-frequency phonon modes are attributed to the vibrations of N atoms, with Si atoms contributing to a lesser extent.

Moreover, to provide further verification of the stability of the $1T'$ - MSi_2N_4 nanosheets at elevated temperatures, we conducted AIMD simulations at both 300 K and 600 K for a duration of 6 ps. To eliminate the size constraint, we utilized the exact supercell dimensions that were previously considered in the phonon spectrum analysis. Plotting the energy fluctuations of the systems enables us to monitor the changes in crystalline morphology, as the total energy of the monolayers is sensitive to any bond breaking and geometry reconstruction at elevated temperatures. The variations of gradient values of the total energies

during the AIMD simulations are illustrated in Fig.3 and the final snapshots of the resulting atomic configurations taken at 300 K and 600 K are shown in the insets. According to the outcomes of AIMD simulations, gradient values for total energies oscillate around a constant value without any sudden changes. From a geometrical perspective, apart from minor distortions of atoms in the vicinity of their thermal equilibrium positions, that are not significant enough to rupture the bonds between the constituent elements, the crystalline configurations of $1T'$ -RuSi₂N₄ and $1T'$ -OsSi₂N₄ are preserved even at elevated temperatures, providing evidence of their thermal stability. The ability of the proposed crystals to withstand elevated temperatures is crucial for their utilization in thermoelectric devices, which often operate under high-temperature conditions.

For the stable single layers, $1T'$ -RuSi₂N₄ and $1T'$ -OsSi₂N₄, we also calculated the Raman activity of each optical vibrational mode at the Γ point [Fig.4(a)]. Raman scattering is one of the most common techniques for acquiring information about the lattice vibrations of a crystal. In the Raman scattering process for a material, an incident photon interacts with the crystal, and subsequently, the scattered photon is promptly collected and analyzed. As a result, the photon either loses energy (Stokes) or gains energy (anti-Stokes) due to interactions with the crystal's phonons. The Raman spectrum of the material is determined by the dispersion of the collected photons with respect to the frequency shift. This type of Raman process is known as a first-order Raman process. From the theoretical standpoint, within the constraints of the momentum conservation, only the phonon with wavevector of $q \sim 0$ (at Γ point) is able to contribute to the first-order Raman activity. Raman spectra of $1T'$ -RuSi₂N₄ and $1T'$ -OsSi₂N₄ exhibit seven and six prominent Raman intensities (labeled with numbers), respectively, indicating that they are observable in a Raman measurement. To elucidate the vibrational properties of the $1T'$ -MSi₂N₄ nanosheets, the motions of the atoms in the optical segment of the vibrational spectrum of $1T'$ -RuSi₂N₄ and $1T'$ -OsSi₂N₄ monolayers are shown in Fig. 4(b) and Fig. S5 of the Supplemental Material [55], respectively. Since the $1T'$ systems are constructed using a 1×2 superlattice, they can be regarded as consisting of right and left RuSi₂N₄ pairs, denoted by the letters L and R, respectively. The I-peak is mostly dominated by the opposite out-of-plane vibration of Ru atoms. For the Raman mode labeled as II, all atoms in the primitive cell vibrate along different directions, with the dominant vibrations coming from the Ru and Si atoms. For the III-peak, the dominant vibration is the out-of-plane motion of the boundary N atoms against each

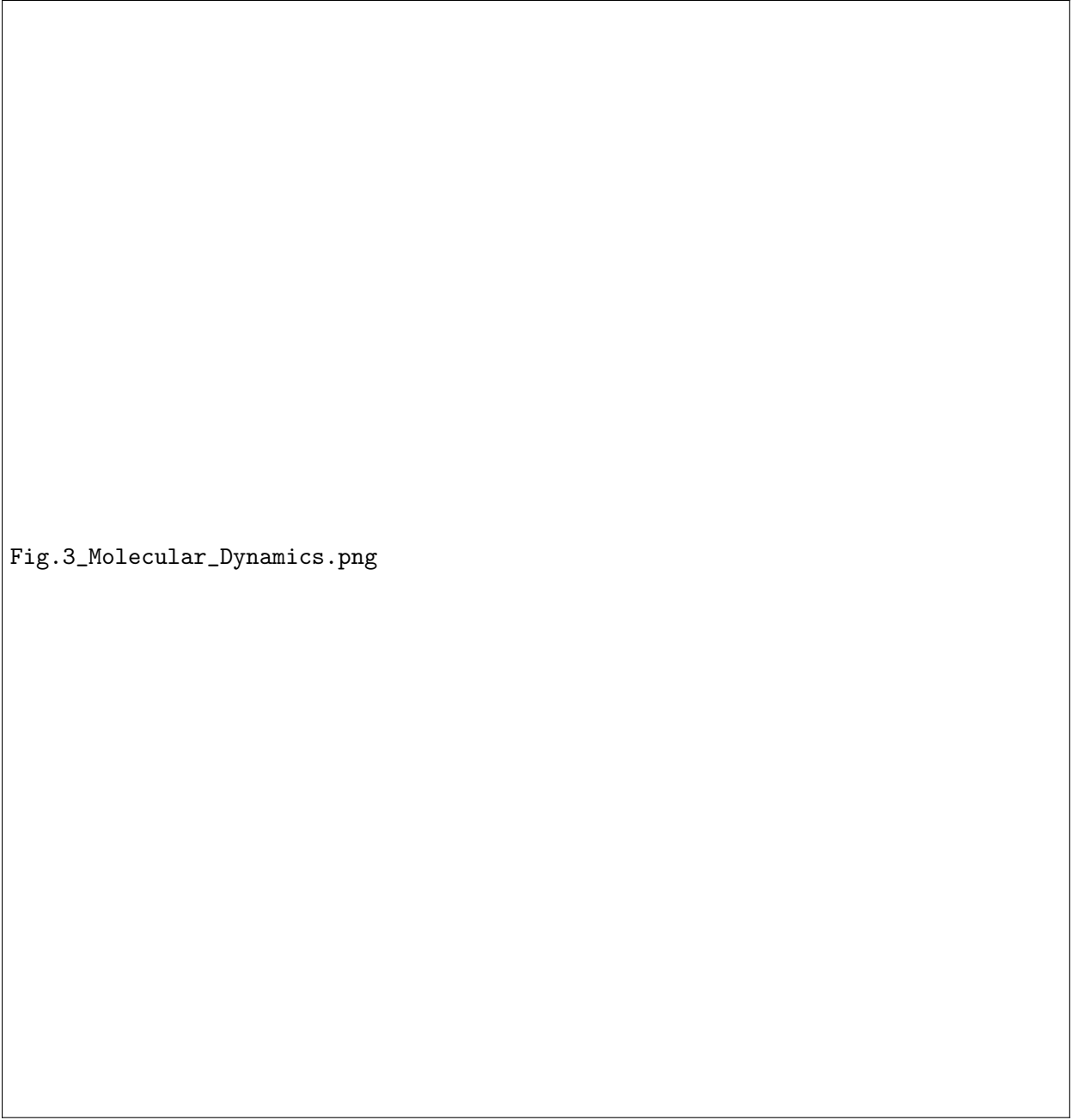


Fig.3_Molecular_Dynamics.png

FIG. 3. The variations of gradient values of the total energies for (a) $1T'$ - RuSi_2N_4 and (b) $1T'$ - OsSi_2N_4 monolayers with respect to the simulation time at 300 and 600 K. The insets illustrate the ultimate snapshot of atomic arrangements at the end of the simulation. E_0 and E represent the total energies of the systems at 0 K and elevated temperatures (300 and 600 K), respectively.

other. The phonon mode VI arises from the mixed vibration of all atoms in the unit cell, with the atomic vibrations of the N atoms in the L pair being more dominant. The V-peak is mainly attributed to the strong out-of-plane vibration of the boundary N atoms in the L pair against each other. The VI- and VII-peaks mainly originate from the out-of-plane vibrations of the inner N atoms in the R and L pairs, respectively. Hereby, the computed Raman spectrum and the peak positions of Raman-active modes can be effectively utilized to characterize the $1T'$ - MSi_2N_4 nanosheets.

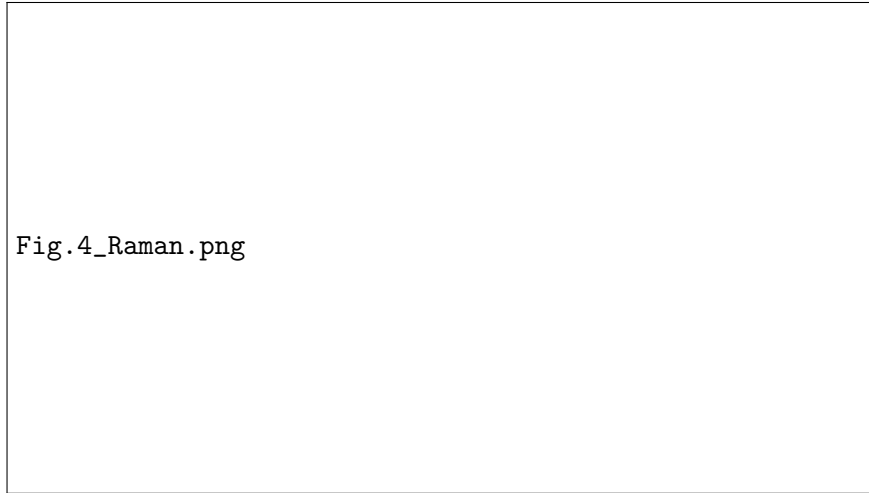


FIG. 4. (a) The calculated Raman activity spectra of the $1T'$ - $RuSi_2N_4$ and $1T'$ - $OsSi_2N_4$ monolayers. (b) The corresponding atomic displacements in some of the prominent Raman active modes for the $1T'$ - $RuSi_2N_4$ monolayer.

C. Elastic Properties

After revealing the dynamical and thermal stability of $1T'$ - $RuSi_2N_4$ and $1T'$ - $OsSi_2N_4$ monolayers, their elastic-strain tensor elements (C_{ij}) are computed to investigate their mechanical stability and elastic properties. In the 2D $1T'$ structures, four non-zero elastic constants should be evaluated, which are C_{11} , C_{22} , C_{12} , and C_{66} . The calculated C_{ij} are listed in the Table II. The calculated elastic constants satisfy the Born-Huang elastic stability criteria [64, 65] [$C_{11}C_{22} - C_{12}^2 > 0$ and $C_{66} > 0$] for 2D rectangular lattice, verifying the mechanical stability. Having secured that $1T'$ - $RuSi_2N_4$ and $1T'$ - $OsSi_2N_4$ crystals possess energetic, dynamical, thermal, and mechanical stability, we proceeded to investigate

the mechanical response of these materials, particularly in terms of in-plane stiffness (or 2D Young's modulus, Y_{2D}), Poisson's ratio (ν), and ultimate tensile strain (UTS). Due to the anisotropic geometry of the structures, it is expected that they exhibit orientation-dependent elastic properties. The orientation-dependent Y_{2D} and ν can be obtained using the formulas given below;

$$Y_{2D}(\theta) = \frac{C_{11}C_{22} - C_{12}^2}{C_{11}s^4 + C_{22}c^4 + \left(\frac{C_{11}C_{22} - C_{12}^2}{C_{66}} - 2C_{12}\right)s^2c^2} \quad (2)$$

$$\nu(\theta) = \frac{C_{12}(s^4 + c^4) - \left(C_{11} + C_{22} - \frac{C_{11}C_{22} - C_{12}^2}{C_{66}}\right)s^2c^2}{C_{11}s^4 + C_{22}c^4 + \left(\frac{C_{11}C_{22} - C_{12}^2}{C_{66}} - 2C_{12}\right)s^2c^2} \quad (3)$$

where s and c stand for $\sin(\theta)$ and $\cos(\theta)$, respectively. The diagram of $Y_{2D}(\theta)$ as θ spans a whole 360° circle is displayed in Fig.5(a). The Y_{2D} , which is defined as the measure of stiffness or flexibility of a 2D material is calculated to be 358 and 369 N/m for the x and y directions, respectively, for $1T'$ -RuSi₂N₄ monolayer, while these values are found to be 343 and 363 N/m for $1T'$ -OsSi₂N₄. The highest value of Y_{2D} for $1T'$ -RuSi₂N₄ and $1T'$ -OsSi₂N₄ monolayers are estimated as 443 and 449 N/m, respectively, at $\theta = 45^\circ$. The directional anisotropy profiles of Y_{2D} in the studied systems are similar; however, in $1T'$ -OsSi₂N₄, it is more pronounced as atomic bond lengths between Os and N atoms (d_{Os-N}) are slightly longer than d_{Ru-N} . As compared to similar $1T'$ crystals, the proposed systems are more flexible than the $1T'$ -WSi₂N₄ nanosheet ($Y_{2D}^{\min} = 452$ and $Y_{2D}^{\max} = 485$ N/m), but stiffer than the $1T'$ -WGe₂N₄ monolayer, with the maximum (minimum) value of 368 (303) N/m [34]. For 2D ultrathin materials, large and anisotropic elastic constants and in-plane stiffness are highly desirable for a wide range of applications, particularly in elastic energy storage. Next, $\nu(\theta)$, which can be defined as the negative ratio of transverse contraction strain to longitudinal extension strain in the direction of the applied stretching force, is calculated and presented in Fig.5(b). The numerical values of ν in the x and y directions (ν^x and ν^y), along with the minimum/maximum value obtained (ν^{\min}/ν^{\max}), are summarized in Table II. ν^x / ν^y are found to be 0.37/0.38 and 0.37/0.40 for single-layers $1T'$ -RuSi₂N₄ and $1T'$ -OsSi₂N₄, respectively. The $\nu(\theta)$ evolution in both systems is similar to each other, with a maximum along y direction and minimum at median angles with respect to principal axes ($\theta = 45^\circ$). The variations of $\nu(\theta)$ within $1T'$ -OsSi₂N₄ monolayer are more evident than those in $1T'$ -RuSi₂N₄, indicating a higher level of anisotropy in the Os-based system. We

also investigated the ultimate tensile strain (UTS), which is another essential intrinsic mechanical property of 2D ultrathin materials. UTS is the maximum value of tensile strain that a material can withstand before its failure. Strain is typically present in experiments, whether it is intentionally introduced or occurs intrinsically. In the process of strain engineering for a 2D material, the structure can be subjected to extreme strains. Whenever a material lacks sufficient strength to tolerate high levels of strain, its structural integrity can be damaged under severe deformation, and the expected performance cannot be achieved. Thus, materials possessing high UTS are typically favored for applications where the ability to withstand maximum loads and ensure durability is crucial. In 2D materials, an applied strain can be calculated by the following expression;

$$\epsilon = \frac{\mathbf{a} - \mathbf{a}_0}{\mathbf{a}_0} \quad (4)$$

where \mathbf{a} and \mathbf{a}_0 represent the lengths of the lattice constants for the strained and unstrained structures along the direction of strain, respectively. Based on Eq.4, uniaxial- x , uniaxial- y , and biaxial strains were induced to the $1T'$ - MSi_2N_4 monolayers. To estimate UTS, a $3 \times 3 \times 1$ supercell is initially constructed to reduce the artificial effects stemming from a small unit cell size, and then the amount of stress imposed into the system under various types of tensile strain is measured. The calculated UTS values of the $1T'$ compounds for applied strains along x (UTS^x), y (UTS^y), and xy (UTS^{xy}) directions are listed in Table II. In addition, the obtained stress-strain curves for $1T'$ - $RuSi_2N_4$ and $1T'$ - $OsSi_2N_4$ nanosheets are shown in Figs. 5(c) and 5(d), respectively. It can be observed that in both systems up to approximately 9%, the stress rate is proportional to the strain and the stress-strain curve remains linear, indicating the elastic regime's range. After this threshold, the range of plastic deformation begins. Within this regime, as the applied tensile strain increases, in-plane stress steadily rises until it reaches the maximum stress level. For $1T'$ - $RuSi_2N_4$ monolayer, UTS^x , UTS^y , and UTS^{xy} are found to be 22%, 17%, and 13%, respectively. Similarly, for the $1T'$ - $OsSi_2N_4$ structure, UTS is achieved at 22%, 17%, and 14% uniaxial- x , uniaxial- y , and equi-biaxial strain levels, respectively. In both crystals, the fracture strain point occurs earlier along the y direction than that of x direction which is due to the quasi-1D nature of the crystal lattice. For the sake of comparison, the ultimate strain for $1H$ - $MoSi_2N_4$ monolayer is obtained at 19.5% [66]. A larger plastic deformation range under biaxial strain is observed for $1T'$ - $RuSi_2N_4$ compared to $1T'$ - $OsSi_2N_4$, which is coherent with the more

pronounced ionic character of Os–N bonds relative to Ru–N bonds. This aligns with the smaller maximum tensile strain exhibited by $1T'$ -RuSi₂N₄ monolayer.

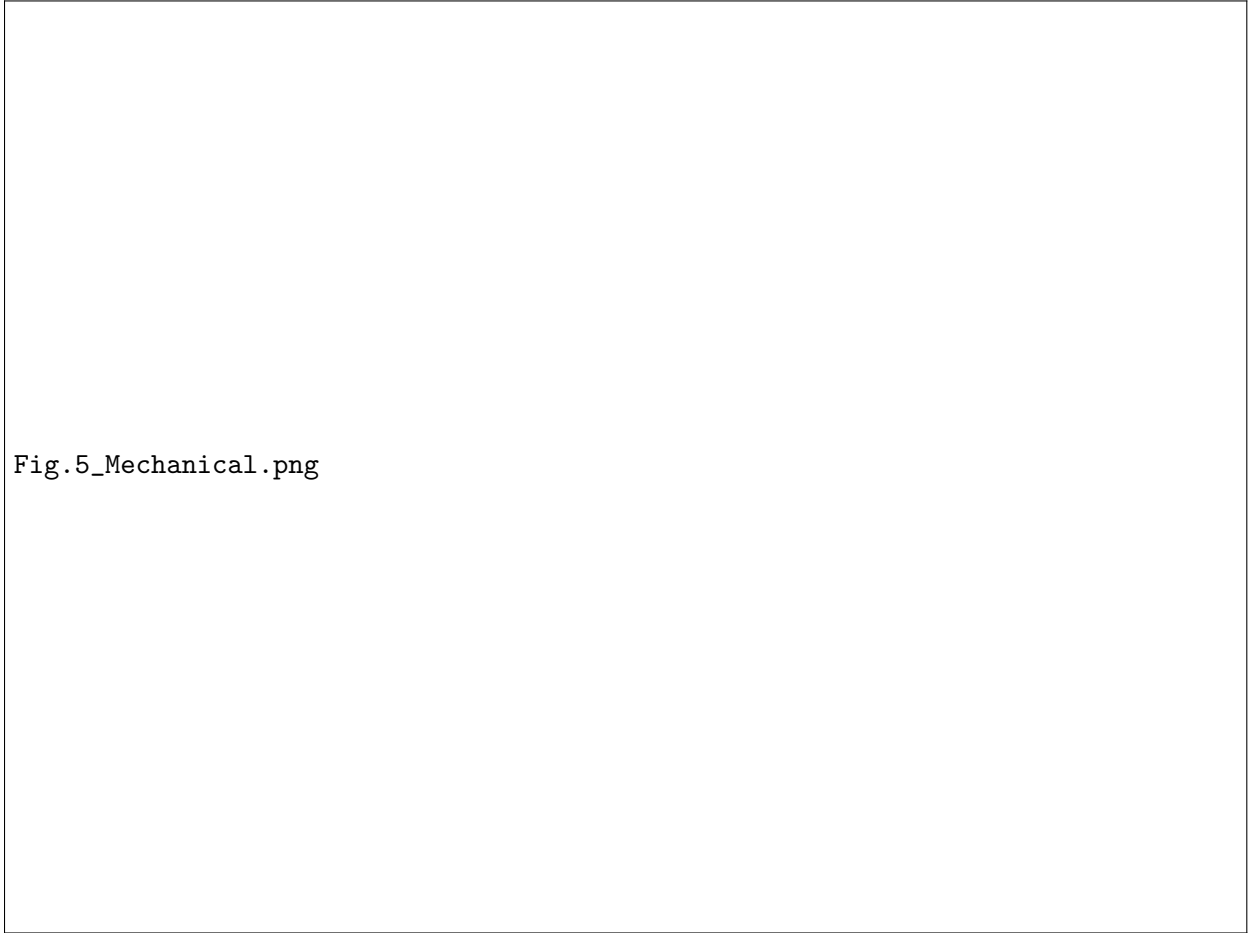


FIG. 5. The schematic diagram of the orientation-dependent elastic properties, (a) in-plane stiffness (Y_{2D}) and (b) Poisson’s ratio (ν), and the variation of stress as a function of biaxial and uniaxial (x and y directions) strains for (c) $1T'$ -RuSi₂N₄ and (d) $1T'$ -OsSi₂N₄ nanosheets.

D. Electronic Properties

Next, we investigate the electronic properties of the RuSi₂N₄ and OsSi₂N₄ systems (for $1T$ and $1T'$ phases). The computed electronic band structures and the orbital-projected density of states (PDOS) are displayed in Fig.6. The electronic band structures are initially calculated using the GGA-PBE functional. It is evident that the $1T$ -MSi₂N₄ structures exhibit ferromagnetic metallic characteristics, with M - d and N- p states crossing the Fermi

TABLE II. For the $1T'$ -RuSi₂N₄ and $1T'$ -OsSi₂N₄ monolayers, relaxed-ion elastic coefficients, C_{ij} , in-plane stiffness, Y_{2D} , Poisson's ratio, ν , and ultimate tensile strain (UTS).

Crystal	C_{11}	C_{22}	C_{12}	C_{66}	Y_{2D}^x	Y_{2D}^y	Y_{2D}^{\max}	ν^x	ν^y	ν^{\min}/ν^{\max}	UTS^x	UTS^y	UTS^{xy}
Structure	(N/m)	(N/m)	(N/m)	(N/m)	(N/m)	(N/m)	(N/m)	(-)	(-)	(-)	(%)	(%)	(%)
$1T'$ -RuSi ₂ N ₄	416	428	156	179	358	369	443	0.37	0.38	0.23/0.38	22	17	13
$1T'$ -OsSi ₂ N ₄	403	426	159	184	343	363	449	0.37	0.40	0.21/0.40	22	17	14

level and a net magnetic moment. On the other hand, it is computed that the $1T'$ -MSi₂N₄ monolayers are nonmagnetic materials and exhibit indirect bandgap semiconductor properties. A similar electronic transition has also been reported for various TMDs [13, 18, 67]. The calculated energy bandgaps at the level of GGA-PBE (E_g^{PBE}) are found to be 0.27 and 0.34 eV for $1T'$ -RuSi₂N₄ and $1T'$ -OsSi₂N₄ monolayers, respectively. In both $1T'$ crystals, the locations of the conduction band minimum (CBM) and valence band maximum (VBM) are situated around the Γ -S and Γ points in the band structure, respectively. The metallic $1T$ structures are prone to instability and transform to stable semiconducting $1T'$ phases. Since the Peierls distortion is a metal-semiconductor transition in quasi-one dimension, this type of phase transition also takes place in the present study. Upon repeating the calculations with the hybrid functional HSE06, we obtained wider energy band gaps (E_g^{HSE}) compared to PBE calculations which is attributed to the shifting of the conduction bands to higher energy values. Nevertheless, the band structure profiles remained unchanged. The acquired E_g^{HSE} values for the $1T'$ -RuSi₂N₄ and $1T'$ -OsSi₂N₄ monolayers are 1.40 eV and 1.47 eV, respectively. These values fall within the infrared part of the optical spectrum. As a comparison, for single-layer T' -MoSi₂N₄ and T' -WSi₂N₄ structures, E_g^{HSE} is reported to be 0.06 and 0.13 eV, respectively [34]. To analyze the contribution of the orbitals to the electronic band structures of the $1T'$ nanosheets, the projected density of states (PDOS) is calculated, and the corresponding results are presented on the right side of the electronic band diagrams. As can be seen, the major contribution to the VBM and CBM comes from the d orbitals of M (Ru, Os) atoms and p orbitals of N atoms. A minor contribution arises from the p orbitals of Si atoms at the upper part of the Fermi level and M - p orbitals below the Fermi level.

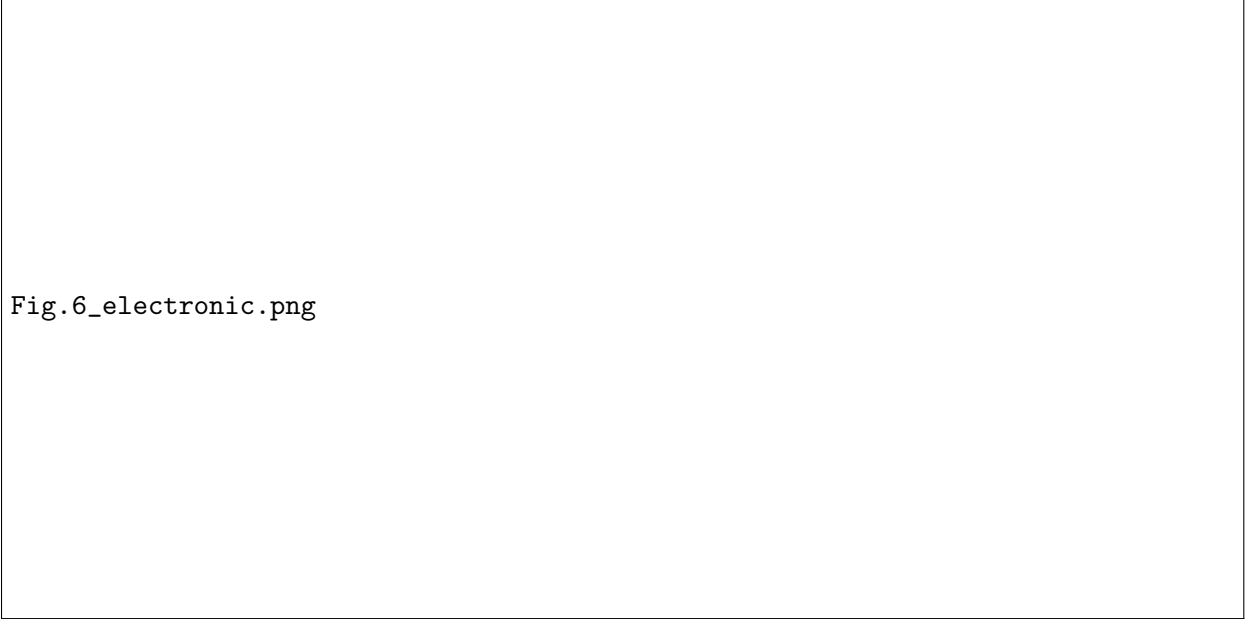


Fig.6_electronic.png

FIG. 6. The electronic band structure and the corresponding orbital projected density of states (PDOS) of $1T$ - and $1T'$ - MSi_2N_4 structures. Two-dimensional Brillouin zones of both phases are also displayed at the insets.

E. Optical Properties

Lastly, the optical properties of stable $1T'$ - MSi_2N_4 structures are investigated. The transition of electrons between the valence band and the conduction band is a crucial absorption process in semiconductors, particularly for their applications in optoelectronic devices. When a specific wavelength of light illuminates a semiconductor material, electrons absorb a certain amount of energy (photon) to propagate across the forbidden band. This transition results in the electron shifting from a low-energy state to a high-energy state. The optical response of 2D materials can be determined by examining the frequency-dependent complex dielectric function, $\varepsilon(\omega)$, which depends on the interaction between electrons and photons under electromagnetic radiation and can be formulated as $[\varepsilon(\omega) = \varepsilon_1(\omega) + i\varepsilon_2(\omega)]$. The imaginary part of the dielectric function $[\varepsilon_2(\omega)]$ can be calculated according to the momentum matrix element between occupied and unoccupied wave functions, while the real part $[\varepsilon_1(\omega)]$ can be estimated from $\varepsilon_2(\omega)$ using the Kramers-Kronig relations. Once the dielectric function is obtained, a variety of optical properties such as absorbance and absorption coefficient can be derived from it. The direction-dependent variation of $\varepsilon_2(\omega)$ with photon

energy for in-plane light polarization in $1T'$ - MSi_2N_4 monolayers, calculated within PBE and HSE06 functionals, is presented in Fig. 7. The anisotropic structure of the $1T'$ nanosheets is also mirrored in the optical absorption. The anisotropic optical response of these systems is desirable for optoelectronic devices because it enables the manipulation of light propagation properties, such as reflection, refraction, and phase velocity. The first peak of the spectrum in the x and y directions for the $1T'$ - $RuSi_2N_4$ (OSi_2N_4) monolayer is located within the visible light range, approximately at 2.09 and 2.41 eV (2.10 and 2.86 eV) respectively. This aligns with the direct electronic bandgap of the crystals. According to the computed imaginary part of the dielectric function, the primary peak corresponds to the transition from the VB to the CB states. Consequently, the energy values mentioned above are ascribed to the fundamental bandgap of the designed nanostructures. By examining the plots of $\epsilon_2(\omega)$ and the orbital-projected density of states for both $1T'$ - MSi_2N_4 nanosheets, the obtained energy values are mainly attributed to the interband transitions from d orbitals of M atoms and p orbitals of N atoms in VBM to $M-d$ and N- p orbitals in CBM. Furthermore, as illustrated in the figure, the initial absorption peak in both materials occurs within the visible light spectrum, while the second peak remains in the near-UV region. These materials with high optical capabilities in both the visible and ultraviolet spectral ranges, are promising candidates for applications in visible-light solar harvesting and utilization, as well as for use in UV sensing devices.

IV. CONCLUSION

In conclusion, inspired by the recent synthesis of high-quality $MoSi_2N_4$ and WSi_2N_4 crystals, we conducted an investigation into the stability and fundamental properties of $1H$ -, $1T$ -, and $1T'$ -phases of MSi_2N_4 ($M = Ru$ and Os) nanosheets through first-principles calculations. The obtained results of cohesive energies (E_C) suggest that the $1T'$ structures are both energetically and structurally more stable than their $1H$ and $1T$ counterparts. Our vibrational frequency analysis revealed that, while the MSi_2N_4 monolayers are dynamically stable in their distorted $1T'$ phase, the phonon spectra of the $1H$ and $1T$ phases exhibit imaginary phonon modes, indicating their dynamical instability. The results of *ab initio* molecular dynamics simulations indicate that the $1T'$ - MSi_2N_4 nanosheets can maintain their structural integrity at elevated temperatures, even up to 600 K, confirming their thermal stability. The

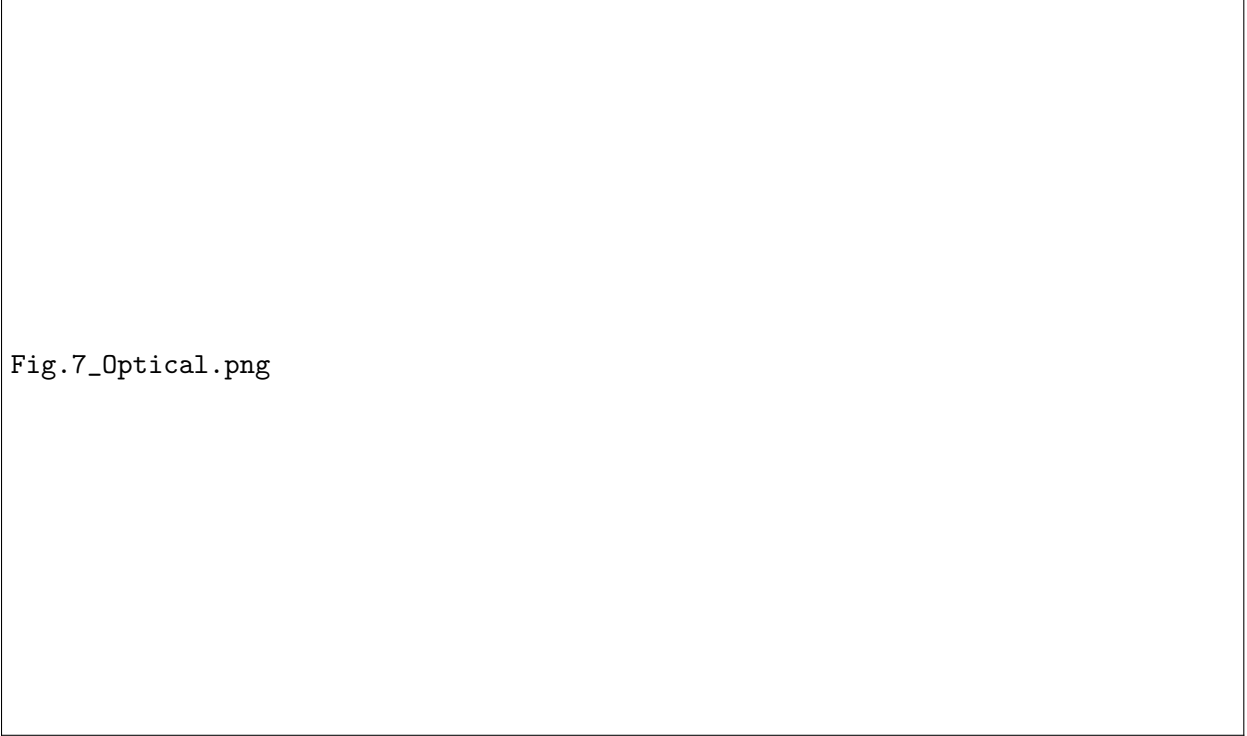


Fig.7_Optical.png

FIG. 7. Direction-dependent variation of the imaginary part $[\varepsilon_2(\omega)]$ of the dielectric function versus photon energy for in-plane polarization in $1T'$ - MSi_2N_4 monolayers. The red and blue lines represent computations based on the GGA-PBE and HSE06 functionals, respectively.

analysis of mechanical properties shows that, owing to the intrinsic structural anisotropy, the $1T'$ - MSi_2N_4 monolayers exhibit direction-dependent in-plane stiffness (Y_{2D}), Poisson's ratio (ν), and ultimate tensile strain (UTS). The 2D $1T'$ crystals exhibit large values of Y_{2D} in different orientations and own high UTS, particularly under uniaxial- x strains, indicating their rigidity and suitability for strain engineering. It was found that, while the $1T$ - MSi_2N_4 monolayers exhibit a ferromagnetic metallic character, $1T'$ phases possess a nonmagnetic semiconducting ground state. The calculated electronic band structure at the level of HSE06 reveals that $1T'$ - $RuSi_2N_4$ and $1T'$ - $OsSi_2N_4$ monolayers have indirect band gaps of 1.40 eV and 1.47 eV, respectively. Additionally, the analysis of optical properties demonstrated that the $1T'$ systems exhibit direction-dependent high light absorption within the visible and near-ultraviolet regions of the spectrum. Our study reveals that the proposed $1T'$ - MSi_2N_4 nanostructures are promising materials for optoelectronic applications, given their enhanced mechanical, electronic, and optical properties.

V. ACKNOWLEDGEMENT

We acknowledge the CINECA award under the ISCRA initiative, for the availability of high-performance computing resources and support. Access to their supercomputing resources was granted through ISCRA class B and C. M.J.V. specifically acknowledges the utilization of EuroHPC resources at the CINECA Supercomputing Centre in Italy (through Project No. EHPC-BEN-2023B09-015 and EHPC-BEN-2024B03-052).

- [1] K. S. Novoselov, A. K. Geim, S. V. Morozov, D.-e. Jiang, Y. Zhang, S. V. Dubonos, I. V. Grigorieva, and A. A. Firsov, Electric field effect in atomically thin carbon films, *Science* **306**, 666 (2004).
- [2] C. Tan, X. Cao, X.-J. Wu, Q. He, J. Yang, X. Zhang, J. Chen, W. Zhao, S. Han, G.-H. Nam, *et al.*, Recent advances in ultrathin two-dimensional nanomaterials, *Chem. Rev.* **117**, 6225 (2017).
- [3] K. Khan, A. K. Tareen, M. Aslam, R. Wang, Y. Zhang, A. Mahmood, Z. Ouyang, H. Zhang, and Z. Guo, Recent developments in emerging two-dimensional materials and their applications, *J. Mater. Chem. C* **8**, 387 (2020).
- [4] S. Z. Butler, S. M. Hollen, L. Cao, Y. Cui, J. A. Gupta, H. R. Gutiérrez, T. F. Heinz, S. S. Hong, J. Huang, A. F. Ismach, *et al.*, Progress, challenges, and opportunities in two-dimensional materials beyond graphene, *ACS Nano* **7**, 2898 (2013).
- [5] P. Miró, M. Audiffred, and T. Heine, An atlas of two-dimensional materials, *Chem. Soc. Rev.* **43**, 6537 (2014).
- [6] K. F. Mak, C. Lee, J. Hone, J. Shan, and T. F. Heinz, Atomically thin MoS₂: a new direct-gap semiconductor, *Phys. Rev. Lett.* **105**, 136805 (2010).
- [7] F. Wu, C. Huang, H. Wu, C. Lee, K. Deng, E. Kan, and P. Jena, Atomically thin transition-metal dinitrides: high-temperature ferromagnetism and half-metallicity, *Nano Lett.* **15**, 8277 (2015).
- [8] H. Wang, J. Li, K. Li, Y. Lin, J. Chen, L. Gao, V. Nicolosi, X. Xiao, and J.-M. Lee, Transition metal nitrides for electrochemical energy applications, *Chem. Soc. Rev.* **50**, 1354 (2021).

- [9] W. Choi, N. Choudhary, G. H. Han, J. Park, D. Akinwande, and Y. H. Lee, Recent development of two-dimensional transition metal dichalcogenides and their applications, *Mater. Today* **20**, 116 (2017).
- [10] J. Ye, Y. J. Zhang, R. Akashi, M. S. Bahramy, R. Arita, and Y. Iwasa, Superconducting dome in a gate-tuned band insulator, *Science* **338**, 1193 (2012).
- [11] D. Costanzo, S. Jo, H. Berger, and A. F. Morpurgo, Gate-induced superconductivity in atomically thin MoS₂ crystals, *Nat. Nanotechnol.* **11**, 339 (2016).
- [12] Y. Li, K.-A. N. Duerloo, K. Wauson, and E. J. Reed, Structural semiconductor-to-semimetal phase transition in two-dimensional materials induced by electrostatic gating, *Nat. Commun.* **7**, 10671 (2016).
- [13] M. J. Varjovi, M. Yagmurcukardes, F. Peeters, and E. Durgun, Janus two-dimensional transition metal dichalcogenide oxides: First-principles investigation of WXO monolayers with X= S, Se, and Te, *Phys. Rev. B* **103**, 195438 (2021).
- [14] C. Chen, X. Ji, K. Xu, B. Zhang, L. Miao, and J. Jiang, Prediction of T- and H-phase two-dimensional transition-metal carbides/nitrides and their semiconducting–metallic phase transition, *ChemPhysChem* **18**, 1897 (2017).
- [15] C. Ataca, H. Sahin, and S. Ciraci, Stable, single-layer MX₂ transition-metal oxides and dichalcogenides in a honeycomb-like structure, *J. Phys. Chem. C* **116**, 8983 (2012).
- [16] K. Chen, J. Deng, Q. Shi, X. Ding, J. Sun, S. Yang, and J. Z. Liu, Charge doping induced reversible multistep structural phase transitions and electromechanical actuation in two-dimensional 1T′-MoS₂, *Nanoscale* **12**, 12541 (2020).
- [17] D. Lin, S. Li, J. Wen, H. Berger, L. Forró, H. Zhou, S. Jia, T. Taniguchi, K. Watanabe, X. Xi, *et al.*, Patterns and driving forces of dimensionality-dependent charge density waves in 2 h-type transition metal dichalcogenides, *Nature communications* **11**, 2406 (2020).
- [18] F. Ersan, S. Cahangirov, G. Gökoğlu, A. Rubio, and E. Aktürk, Stable monolayer honeycomb-like structures of RuX₂ (X= S, Se), *Phys. Rev. B* **94**, 155415 (2016).
- [19] Y.-L. Hong, Z. Liu, L. Wang, T. Zhou, W. Ma, C. Xu, S. Feng, L. Chen, M.-L. Chen, D.-M. Sun, *et al.*, Chemical vapor deposition of layered two-dimensional MoSi₂N₄ materials, *Science* **369**, 670 (2020).
- [20] A. Priyadarshi, Y. S. Chauhan, S. Bhowmick, and A. Agarwal, Large and anisotropic carrier mobility in monolayers of the MA₂Z₄ series (M = Cr, Mo, W; A = Si, Ge; and Z = N, P),

- Nanoscale **14**, 11988 (2022).
- [21] K. S. Novoselov, Discovery of 2D van der waals layered MoSi_2N_4 family, Natl. Sci. Rev. **7**, 1842 (2020).
- [22] M. J. Varjovi, S. Ershadrad, B. Sanyal, and S. Tosoni, Two-dimensional MSi_2N_4 ($\text{M} = \text{Ge}, \text{Sn}$, and Pb) monolayers: promising new materials for optoelectronic applications, 2d Mater. **11**, 015016 (2023).
- [23] B. Mortazavi, B. Javvaji, F. Shojaei, T. Rabczuk, A. V. Shapeev, and X. Zhuang, Exceptional piezoelectricity, high thermal conductivity and stiffness and promising photocatalysis in two-dimensional MoSi_2N_4 family confirmed by first-principles, Nano Energy **82**, 105716 (2021).
- [24] Y. Yin, Q. Gong, M. Yi, and W. Guo, Emerging versatile two-dimensional MoSi_2N_4 family, Adv. Funct. Mater. **33**, 2214050 (2023).
- [25] M. J. Varjovi, M. E. Kilic, and E. Durgun, First-principles investigation on the structural, vibrational, mechanical, electronic, and optical properties of MSi_2Z_4 (M : Pd and Pt , Z : N and P) monolayers, Phys. Rev. Mater. **7**, 034002 (2023).
- [26] L. Wang, Y. Jiang, J. Liu, S. Zhang, J. Li, P. Liu, Y. Sun, H. Weng, and X.-Q. Chen, Two-dimensional obstructed atomic insulators with fractional corner charge in the MA_2Z_4 family, Phys. Rev. B **106**, 155144 (2022).
- [27] W. Zhang, W. Yang, Y. Liu, Z. Liu, and F. Zhang, Computational exploration and screening of novel Janus MA_2Z_4 ($\text{M} = \text{Sc-Zn}, \text{Y-Ag}, \text{Hf-Au}$; $\text{A} = \text{Si}, \text{Ge}$; $\text{Z} = \text{N}, \text{P}$) monolayers and potential application as a photocatalyst, Front. Phys. **17**, 63509 (2022).
- [28] J. Zeng, L. Xu, X. Luo, T. Chen, S.-H. Tang, X. Huang, and L.-L. Wang, Z-scheme systems of ASi_2N_4 ($\text{A} = \text{Mo}$ or W) for photocatalytic water splitting and nanogenerators, Tungsten , 1 (2021).
- [29] Z. Zhao, X. Duan, X. Fang, X. Wang, and W. Mi, Prediction of electronic structure and magnetic anisotropy of two-dimensional MSi_2N_4 ($\text{M} = 3\text{d}$ transition-metal) monolayers, Appl. Surf. Sci. **611**, 155693 (2023).
- [30] M. Jahangirzadeh Varjovi, M. E. Kilic, and E. Durgun, A first-principles investigation of insin2 monolayer: A novel two-dimensional material with enhanced stability and tunable vibrational and electronic properties, The Journal of Physical Chemistry C (2024).
- [31] L. Wang, Y. Shi, M. Liu, A. Zhang, Y.-L. Hong, R. Li, Q. Gao, M. Chen, W. Ren, H.-M. Cheng, *et al.*, Intercalated architecture of MA_2Z_4 family layered van der waals materials

- with emerging topological, magnetic and superconducting properties, *Nat. Commun.* **12**, 2361 (2021).
- [32] S. Li, W. Wu, X. Feng, S. Guan, W. Feng, Y. Yao, and S. A. Yang, Valley-dependent properties of monolayer MoSi_2N_4 , WSi_2N_4 , and MoSi_2As_4 , *Phys. Rev. B* **102**, 235435 (2020).
- [33] Y. Ding and Y. Wang, Computational exploration of stable 4d/5d transition-metal MSi_2N_4 ($M = \text{Y-Cd}$ and Hf-Hg) nanosheets and their versatile electronic and magnetic properties, *J. Phys. Chem. C* **125**, 19580 (2021).
- [34] Y. Ding and Y. Wang, Two-dimensional T' - phase MA_2N_4 ($M = \text{Mo/W}$, $A = \text{Si/Ge}$) nanosheets: First-principles insights into the structural stability, electronic property and catalytic performance for hydrogen evolution reaction, *Appl. Surf. Sci.* **627**, 157256 (2023).
- [35] X. Cao, J. Huo, L. Li, J. Qu, Y. Zhao, W. Chen, C. Liu, H. Liu, and G. Wang, Recent advances in engineered Ru-based electrocatalysts for the hydrogen/oxygen conversion reactions, *Adv. Energy Mater.* **12**, 2202119 (2022).
- [36] A. Kratzig, C. Zachäus, S. Brunken, D. Thomas, P. Bogdanoff, K. Ellmer, and S. Fiechter, RuS_2 thin films as oxygen-evolving electrocatalyst: Highly oriented growth on single-crystal FeS_2 substrate and their properties compared to polycrystalline layers, *Phys. Status Solidi (A)* **211**, 2020 (2014).
- [37] Y. Li, N. Li, K. Yanagisawa, X. Li, and X. Yan, Hydrothermal synthesis of highly crystalline RuS_2 nanoparticles as cathodic catalysts in the methanol fuel cell and hydrochloric acid electrolysis, *Mater. Res. Bull.* **65**, 110 (2015).
- [38] D. Pelclova, Osmium, in *Handbook on the Toxicology of Metals* (Elsevier, 2022) pp. 639–647.
- [39] M. Sarno, E. Ponticorvo, and D. Scarpa, Ru and Os based new electrode for electrochemical flow supercapacitors, *J. Chem. Eng.* **377**, 120050 (2019).
- [40] W. Kohn and L. J. Sham, Self-consistent equations including exchange and correlation effects, *Phys. Rev.* **140**, A1133 (1965).
- [41] P. Hohenberg and W. Kohn, Inhomogeneous electron gas, *Phys. Rev.* **136**, B864 (1964).
- [42] P. E. Blöchl, Projector augmented-wave method, *Phys. Rev. B* **50**, 17953 (1994).
- [43] G. Kresse and J. Hafner, Ab initio molecular dynamics for liquid metals, *Phys. Rev. B* **47**, 558 (1993).
- [44] G. Kresse and J. Hafner, Ab initio molecular-dynamics simulation of the liquid-metal–amorphous-semiconductor transition in germanium, *Phys. Rev. B* **49**, 14251 (1994).

- [45] G. Kresse and J. Furthmüller, Efficiency of ab-initio total energy calculations for metals and semiconductors using a plane-wave basis set, *Comput. Mater. Sci.* **6**, 15 (1996).
- [46] G. Kresse and J. Furthmüller, Efficient iterative schemes for ab initio total-energy calculations using a plane-wave basis set, *Phys. Rev. B* **54**, 11169 (1996).
- [47] J. P. Perdew, K. Burke, and M. Ernzerhof, Generalized gradient approximation made simple, *Phys. Rev. Lett.* **77**, 3865 (1996).
- [48] J. Heyd, G. E. Scuseria, and M. Ernzerhof, Hybrid functionals based on a screened coulomb potential, *J. Chem. Phys.* **118**, 8207 (2003).
- [49] A. V. Krukau, O. A. Vydrov, A. F. Izmaylov, and G. E. Scuseria, Influence of the exchange screening parameter on the performance of screened hybrid functionals, *J. Chem. Phys.* **125**, 224106 (2006).
- [50] H. J. Monkhorst and J. D. Pack, Special points for brillouin-zone integrations, *Phys. Rev. B* **13**, 5188 (1976).
- [51] G. Henkelman, A. Arnaldsson, and H. Jónsson, A fast and robust algorithm for bader decomposition of charge density, *Comput. Mater. Sci.* **36**, 354 (2006).
- [52] A. Togo and I. Tanaka, First principles phonon calculations in materials science, *Scr. Mater.* **108**, 1 (2015).
- [53] A. Fonari and S. Stauffer, *vasp-raman.py* (<https://github.com/raman-sc/VASP/>, 2013).
- [54] M. Calandra, I. Mazin, and F. Mauri, Effect of dimensionality on the charge-density wave in few-layer 2H – NbSe₂, *Phys. Rev. B* **80**, 241108 (2009).
- [55] See Supplemental Material for additional details on Bader charge analyses, planar average of the electrostatic potential diagrams in x , y and z directions for 1H-, 1T-, and 1T'-MSi₂N₄ monolayers, and POSCAR files of relaxed structures of the 1T'-MSi₂N₄ monolayers.
- [56] K. Rossnagel, On the origin of charge-density waves in select layered transition-metal dichalcogenides, *J. Condens. Matter Phys.* **23**, 213001 (2011).
- [57] S. S. Chou, N. Sai, P. Lu, E. N. Coker, S. Liu, K. Artyushkova, T. S. Luk, B. Kaehr, and C. J. Brinker, Understanding catalysis in a multiphase two-dimensional transition metal dichalcogenide, *Nat. Commun.* **6**, 8311 (2015).
- [58] K. Chen, J. Deng, X. Ding, J. Sun, S. Yang, and J. Z. Liu, Ferromagnetism of 1T'-MoS₂ nanoribbons stabilized by edge reconstruction and its periodic variation on nanoribbons width, *J. Am. Chem. Soc.* **140**, 16206 (2018).

- [59] A. Bafekry, M. Faraji, D. Hoat, M. Shahrokhi, M. Fadlallah, F. Shojaei, S. Feghhi, M. Ghergherehchi, and D. Gogova, MoSi₂N₄ single-layer: a novel two-dimensional material with outstanding mechanical, thermal, electronic and optical properties, *J. Phys. D: Appl. Phys* **54**, 155303 (2021).
- [60] X. Ma, H. Bo, X. Gong, G. Yuan, Z. Peng, J. Lu, and Q. Xie, Tunable schottky barrier of WSi₂N₄/graphene heterostructure via interface distance and external electric field, *Appl. Surf. Sci.* , 156385 (2023).
- [61] H. Chen, J. Zhang, D. Kan, J. He, M. Song, J. Pang, S. Wei, and K. Chen, The recent progress of two-dimensional transition metal dichalcogenides and their phase transition, *Crystals* **12**, 1381 (2022).
- [62] Z. Tian, J. Garg, K. Esfarjani, T. Shiga, J. Shiomi, and G. Chen, Phonon conduction in PbSe, PbTe, and PbTe_{1-x}Se_x from first-principles calculations, *Phys. Rev. B* **85**, 184303 (2012).
- [63] F. Warmuth, M. Wormser, and C. Körner, Single phase 3D phononic band gap material, *Sci. Rep.* **7**, 1 (2017).
- [64] M. Born and K. Huang, *Dynamical theory of crystal lattices* (Clarendon press, 1954).
- [65] F. Mouhat and F.-X. Coudert, Necessary and sufficient elastic stability conditions in various crystal systems, *Phys. Rev. B* **90**, 224104 (2014).
- [66] Q. Li, W. Zhou, X. Wan, and J. Zhou, Strain effects on monolayer MoSi₂N₄: ideal strength and failure mechanism, *Phys. E: Low-Dimens. Syst. Nanostructures* **131**, 114753 (2021).
- [67] M. Calandra, Chemically exfoliated single-layer MoS₂: Stability, lattice dynamics, and catalytic adsorption from first principles, *Phys. Rev. B* **88**, 245428 (2013).